



Received November 05, 2024; accepted March 20, 2025; Date of publication April 07, 2025.  
The review of this paper was arranged by Associate Editor Fernanda de M. Carnielutti<sup>✉</sup> and Editor-in-Chief Heverton A. Pereira<sup>✉</sup>.

Digital Object Identifier <http://doi.org/10.18618/REP.e202530>

# Performance Analysis and Comparison Between Predictive Current and Predictive Torque Control Applied to a DFIG-DC System

Lucas F. M. de Lucena<sup>✉1</sup>, Victor F. M. B. Melo<sup>✉2,\*</sup>, Nady Rocha<sup>✉1</sup>,  
Ruben da C. Ferreira<sup>✉1</sup>, Marco Rivera<sup>✉3,4</sup>

<sup>1</sup>Federal University of Paraíba, Electrical Engineering Department, João Pessoa, PB, Brazil.

<sup>2</sup>Federal University of Paraíba, Renewable Energies Engineering Department, João Pessoa, PB, Brazil.

<sup>3</sup>University of Nottingham, Department of Electrical and Electronic Engineering, Faculty of Engineering, United Kingdom.

<sup>4</sup>Talca University, Laboratorio de Conversión de Energías y Electrónica de Potencia, Chile.

e-mail: lucas.lucena@alumni.cear.ufpb.br; victor@cear.ufpb.br\*; nadyrocha@cear.ufpb.br; eng.rubencruz@gmail.com; marco.rivera@nottingham.ac.uk.

\* Corresponding author.

**ABSTRACT** The expansion of DC microgrids has prompted investigations into wind energy systems to harness the benefits of this configuration. Therefore, this study aims to analyze and compare the performances of predictive current control (PCC) and predictive flux and torque control (PTC) applied to a doubly-fed induction generator which has its stator windings connected to a DC microgrid by means of a diode bridge. This system is commonly known as DFIG-DC. The system's performance was evaluated in terms of electromagnetic torque ripple, rotor flux ripple, and current distortion across a range of operating speeds. Although PCC and PTC applied to DFIG-DC have been discussed in previous works, a systematic comparison between them lacks in the literature, which is the main contribution of this paper. In addition, this work discusses the robustness of both methods under parametric errors of stator and rotor resistances, and magnetizing inductance, which has not been approached before.

**KEYWORDS** DC microgrid, doubly-fed induction machine, predictive current control, predictive flux and torque control.

## I. INTRODUCTION

Advances in power electronics technology play a crucial role in facilitating the operation of DC microgrids. When compared with AC microgrids, DC microgrids have the following advantages: they do not need to synchronize the generating sources connected to the bus; they can supply loads of different frequencies using frequency inverters; inductance and capacitance are not present in the DC system, and therefore, the voltage drop is lower, allowing better voltage regulation; they are more efficient because they do not have reactive power and skin effect [1]–[4]. To take advantage of the benefits of this configuration, studies were carried out and implemented on wind energy systems in these grids [1], [4].

Considering the use of doubly-fed induction generators (DFIG), their stator windings are usually connected to the DC microgrids by means of diode-based rectifiers. Meanwhile, the rotor windings are connected to the same microgrid employing a full-controlled converter, which performs the machine control. This system (illustrated in Fig. 1) is named in the literature as DFIG-DC, and has stood out due to its robust performance and independent control for active and reactive power [5], [6]. According to [7], the most prominent applications of DFIG-DC are wind power

generation and interconnection [8], distributed generation and DC microgrids [9], [10], islanded power systems for mines [11], and on-board power generation [12].

Studies show that DFIG-DC can be controlled by different techniques. Reference [13] uses a direct torque control (DTC) scheme based on a hysteresis controller. Reference [14] compares DTC with field-oriented control (FOC) focusing on torque oscillation cancellation. And [15] proposes a simple control technique suitable to regulate the power delivered to the DC grid based on the regulation of the rotor flux linkage.

Also, Finite Control Set-Model Predictive Control (FCS-MPC) has been employed in machine drive systems in general. In this technique, based on the system model, the controlled variables are predicted for each available switching state. In this way, a cost function is determined, and the switching state that minimizes this function is selected and applied, sending its correspondent gating signals to the converter switches [16]. Compared to Proportional-Integral (PI)-based methods, such as FOC, FCS-MPC has the advantages of providing simple multivariable control and straightforward implementation, avoiding the tuning process of PI controllers, and providing faster dynamic response.

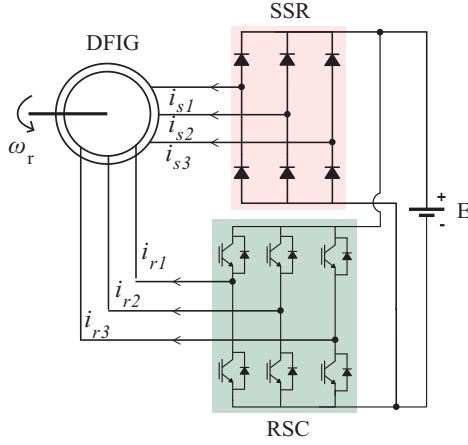


FIGURE 1. Circuit of the DFIG-DC system.

Among the types of FCS-MPC, the most discussed for machine control are the predictive current control (PCC) and the predictive flux and torque control (PTC). Reference [17] compares the performance of PCC and PTC for a three-phase squirrel-cage induction machine (IM). Simulations and experiments were carried out for steady and transient state operation, as well as parametric variation. PCC presented lower current harmonic distortion, but higher torque ripple compared to PTC. Depending on the application, this may be an important advantage of PTC over PCC since, as discussed in [18]–[20], torque pulsations result in torsional vibrations and shaft failures. In this way, it is very important to reduce torque ripple in DFIG-DC or any system that employs electric machines. In addition, [17] also proved that PTC is more robust to an error in estimating the value of the magnetizing inductance of the induction machine. On the other hand, PCC proved to be more robust when there is an error in estimating the resistance of the stator winding.

Also, in [21], four FCS-MPC methods (linear PCC, nonlinear PCC, linear PTC and nonlinear PTC) are compared to control a squirrel-cage induction machine configured in open-end for common mode current suppression. And fault-tolerance performance when applying PCC to a squirrel-cage IM drive was also verified in [22]. It is proved that PCC provides proper postfault operation when the system is submitted to a single-phase open-circuit fault, assuring postfault sinusoidal magnetic flux and low torque ripple.

Regarding the use of DFIG, [23] discussed a FCS-MPC method that regulates real and reactive powers in a conventional type-III wind energy conversion system (WECS). And finally, when it comes to DFIG-DC, [24] proposed a sensorless PCC method that regulates the rotor currents without the need for a position sensor. However, it does not compensate for the delay introduced by the digital processors and does not perform any discussion on torque ripple. And [25] shows an optimized PTC in order to minimize system losses and obtain low torque ripple.

In this context, the present paper discusses the application of PCC and PTC to the DFIG-DC system. This is an extended version of conference paper [26]. The main contributions of this new version are: 1) Deeper discussion of PCC and PTC methods applied to the DFIG-DC system; 2) Comparative analysis between the methods in terms of stator and rotor currents harmonic distortion, torque ripple, flux ripple, and transient response based on simulation and experimental results in different operation scenarios. This comparison has not been done in the literature; 3) Analysis of the robustness of the methods in the presence of parametric errors or variations, which is not present in the literature either.

The paper is divided as follows: Section II presents the mathematical model of the system; Sections III and IV detail the mathematical modeling used for predictive current control and predictive torque and flux control, respectively; In Section V, the selection of the switching state is explained; The simulation and experimental results of the DFIG-DC system comparing PCC and PTC are shown in Section VI and VII respectively; Section VIII presents the conclusion.

## II. SYSTEM MODEL

The mathematical model of the DFIG in the  $dq$  rotor reference frame can be described by [25], [27]:

$$\vec{v}_s^r = r_s \vec{i}_s^r + \frac{d\vec{\lambda}_s^r}{dt} + j\omega_r \vec{\lambda}_s^r \quad (1)$$

$$\vec{v}_r^r = r_r \vec{i}_r^r + \frac{d\vec{\lambda}_r^r}{dt} \quad (2)$$

$$\vec{\lambda}_s^r = l_s \vec{i}_s^r + l_m \vec{i}_r^r \quad (3)$$

$$\vec{\lambda}_r^r = l_r \vec{i}_r^r + l_m \vec{i}_s^r \quad (4)$$

$$T_e = P(i_{rd}^r \lambda_{rq}^r - \lambda_{rd}^r i_{rq}^r) \quad (5)$$

$$T_e - T_m = F_m \omega_r + J_m \frac{d\omega_r}{dt} \quad (6)$$

The subscripts  $s$  and  $r$  represent the stator and rotor parameters, respectively,  $\omega_r$  is the rotor electrical speed,  $r_s$  and  $r_r$  are the stator and rotor resistance, respectively,  $l_s$  and  $l_r$  are the inductances of the stator and rotor windings, respectively,  $l_m$  is magnetizing inductance.  $\vec{v}$ ,  $\vec{i}$  and  $\vec{\lambda}$  are vectors of voltage, current and flux, respectively, where  $\vec{x}_n^r = x_{nd}^r + jx_{nq}^r$  is the vector of variable  $x$  in rotor reference frame with  $x = v, i$  and  $\lambda$ ,  $n = s$  (stator) or  $r$  (rotor), and  $j = \sqrt{-1}$ .  $T_e$  and  $T_m$  are the electromagnetic and mechanical torque, respectively,  $F_m$  is the friction coefficient,  $J_m$  is the moment of inertia,  $P$  is the machine number of pairs of poles.

### A. Speed control and electromagnetic torque reference

The machine speed is regulated using a conventional PI controller. It generates, at its output, the electromagnetic torque reference, which is used to obtain the current references in PCC, and for the cost function in PTC. Considering the mechanical torque as a disturbance, the electromagnetic



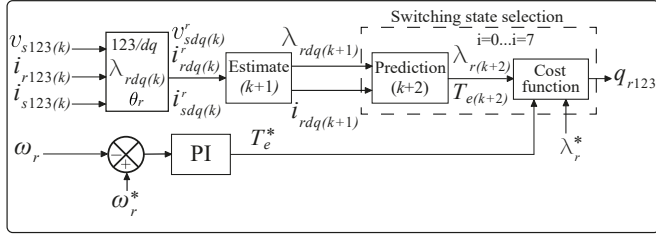


FIGURE 3. PTC control diagram.

in  $k + 2$ , when discretized by forward Euler method and compensating for the delay, are:

$$\lambda_{rd(k+2)}^r = \lambda_{rd(k+1)}^r + (v_{rd(k+2)}^r - r_r i_{rd(k+1)}^r) T_s, \quad (19)$$

$$\lambda_{rq(k+2)}^r = \lambda_{rq(k+1)}^r + (v_{rq(k+2)}^r - r_r i_{rq(k+1)}^r) T_s, \quad (20)$$

where  $\lambda_{rd(k+1)}^r$  and  $\lambda_{rq(k+1)}^r$  come from (12); the currents  $i_{rd(k+1)}^r$  and  $i_{rq(k+1)}^r$  comes from instant  $k + 1$ ;  $v_{rd(k+2)}^r$  and  $v_{rq(k+2)}^r$  are obtained through the switching state of the rotor converter during the commutation tests of the predictive control, as will be explained in Section V. Finally, the predicted rotor flux module is determined by:

$$\lambda_{r(k+2)}^r = \sqrt{\lambda_{rd(k+2)}^r{}^2 + \lambda_{rq(k+2)}^r{}^2}. \quad (21)$$

The electromagnetic torque is calculated through the rotor current and the rotor flux, according to (5). In this way, the prediction of torque is given by

$$T_e(k+2) = P(i_{rd(k+2)}^r \lambda_{rq(k+2)}^r - \lambda_{rd(k+2)}^r i_{rq(k+2)}^r), \quad (22)$$

where  $i_{rd(k+2)}^r$ ,  $i_{rq(k+2)}^r$ ,  $\lambda_{rd(k+2)}^r$  and  $\lambda_{rq(k+2)}^r$  come from the equations (10), (11), (19) and (20), respectively. In PTC, stator voltages used in (10) and (11) are measured directly from the machine by sensors and then transformed into  $dq$  rotor reference frame.

The selected cost function considers two control objectives: 1) Imposing a constant electromagnetic torque; and 2) Regulating the amplitude of the rotor flux. The PTC cost function is based on torque and rotor flux errors and is given by:

$$F_c = (T_e^* - T_e(k+2))^2 + k_\lambda (\lambda_r^* - \lambda_{r(k+2)}^r)^2. \quad (23)$$

In this case, there is a weighting factor for the rotor flux expressed by  $k_\lambda$ . The PTC control diagram is represented in Fig. 3.

## V. SWITCHING STATE SELECTION

For the two-level inverter used in the RSC for PCC and PTC, the switching state voltage is given by  $v_{rd}^r = \sqrt{\frac{2}{3}}(q_{r1} - \frac{q_{r2}}{2} - \frac{q_{r3}}{2})E$  and  $v_{rq}^r = \frac{1}{\sqrt{2}}(q_{r2} - q_{r3})E$ . To determine the predicted control variables for the instant  $k + 2$ , these voltages are inserted into Equations (10), (11), (19) and (20), through the variables  $v_{rd(k+2)}^r$  and  $v_{rq(k+2)}^r$ . After testing all combinations, the voltage vector that minimizes the cost function is applied on the converter switches.

TABLE 1. DFIG parameters.

	Parameters	Values
$P_n$	Rated power	560 W
$r_s$	Stator resistance	15.1 $\Omega$
$l_s$	Stator inductance	563.7 mH
$r_r$	Rotor resistance	6.22 $\Omega$
$l_r$	Rotor inductance	563.7 mH
$l_m$	Magnetizing inductance	523.8 mH
$J_m$	Moment of inertia	0.013 $Kg \cdot m^2$
$F_m$	Viscous friction constant	0.001 $N \cdot sm^2$
$N_s/N_r$	Stator and rotor turns ratio	1.82/1
$\omega_n$	Rated speed	400 rad/s
$P$	Number of pole pairs	1

TABLE 2. System and control parameters used in the simulations.

	Parameters	Values
$E$	DC bus voltage	250 V
$T_s$	Control calculation step	100 $\mu s$
$h$	Simulation calculation step	0.1 $\mu s$
$\tau_s$	Control accommodation time	0.65 s
$\xi$	Damping factor	0.7
$\lambda_r$	Reference rotor flux for PTC	0.93 Wb
$k_\lambda$	Weighting factor for rotor flux	5
$\omega_s$	Synchronous speed for PCC	314 rad/s

## VI. SIMULATION RESULTS

Simulations of the DFIG-DC system were performed using a 560-W DFIG through softwares PSIM<sup>®</sup>, Matlab<sup>®</sup> and DevC++<sup>®</sup>. The values of DFIG, system and control parameters used in the simulations are shown in the Tables 1 and 2, respectively.

Figure 4 shows the steady-state simulation results for PCC and PTC for a speed reference of  $\omega_r^* = 300$  rad/s. Data on speed, torque, rotor flux, rotor currents and stator voltage and current were obtained. Total harmonic distortion (THD), flux and torque ripple were also computed. The THD is calculated by:

$$THD(\%) = \frac{\sqrt{I_{rms}^2 - I_1^2}}{I_1} 100\%, \quad (24)$$

where  $I_{rms}$  is the rms value of the phase current and  $I_1$  is the rms value of the phase current fundamental component.

The ripple is determined by (25), where  $ripple$  is given in percentage;  $N$  is the number of samples;  $x_i$  and  $x_{avg}$  are the values of each sample and the average of the signal, respectively.

$$ripple(\%) = 100 \sqrt{\frac{1}{N} \sum_{i=1}^N (x_i - x_{avg})^2}. \quad (25)$$

Figs. 4(a) and 4(b) show the rotor speed and its reference for PCC and PTC, respectively. Observe that both methods are capable of regulating properly the rotor speed.

It can be seen from Figs. 4(c), for PCC, and 4(d), for PTC, that the torque has an average value of -2N.m, and

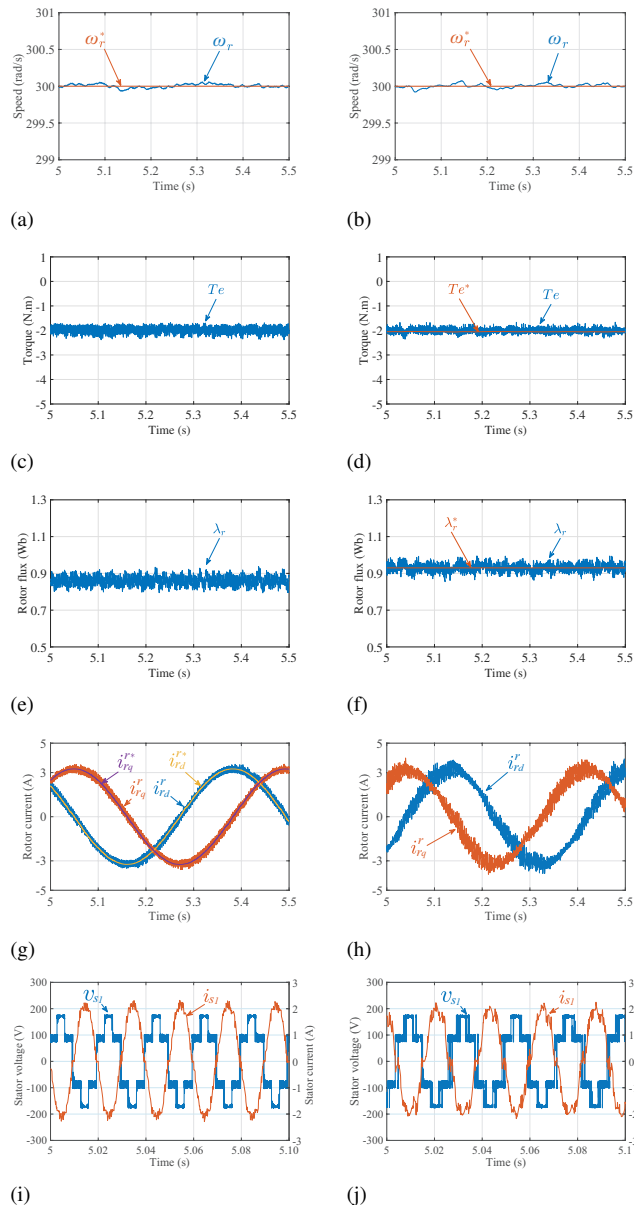


**FIGURE 4.** Simulation results for steady-state predictive control for  $\omega_r = 300$  rad/s. (a) PCC machine speed. (b) PTC machine speed. (c) PCC torque. (d) PTC torque. (e) PCC rotor flux. (f) PTC rotor flux. (g) PCC rotor currents in the rotor reference frame. (h) PTC rotor currents in the rotor reference frame. (i) PCC stator phase voltage and phase current. (j) PTC stator phase voltage and phase current.

that the torque ripple produced by PTC is less than that produced by PCC. The negative value of torque means that the machine operates as generator. Concerning the rotor flux, PTC regulates its value to its reference value (see Fig. 4(f)). And PCC, although it does not directly regulate the rotor flux, provides an average value of around 0.86 Wb, as shown in Fig. 4(e).

Figs. 4(g) and 4(h) show the rotor current in the  $dq$  rotor reference frame. It is evident for PCC that the rotor current closely tracks its reference with low distortion. In contrast, PTC exhibits higher current ripple. Another detail is that the

synchronous frequency is different in each technique. PCC has a fixed synchronous frequency of  $\omega_s = 314$  rad/s (50 Hz). Therefore, it is noted that for the reference speed of 300 rad/s, the PCC is in subsynchronous operating mode. On the other hand, PTC does not have a fixed synchronous frequency, which depends on the point of operation. For this simulation, it is clear that the PTC is in supersynchronous operating mode, since current  $i_{rq}$  leads current  $i_{rd}$ .

The stator voltage and current can be seen in Fig. 4(i) for PCC and Fig. 4(j) for PTC. Note that the currents are  $180^\circ$  out-of-phase with the voltage, as the machine operates as generator with a unity power factor. Furthermore, PCC stator currents have a sinusoidal waveform despite being connected to a diode bridge.

Simulation results for speeds of 270 rad/s and 340 rad/s, as well as simulation THD values, can be seen in [26]. However, torque and flux ripples comparison is shown in Table 3.

Table 3 shows the electromagnetic torque and rotor flux ripple values for three different steady-state speeds ( $\omega_r^* = 270, 300, 340$  rad/s). For all scenarios, PTC obtained a smaller value in both torque and flux ripple. Considering  $\omega_r^* = 300$  rad/s in which PCC obtained the lowest ripple value, PTC presents torque and flux ripple 36.48% and 18.80% lower than PCC, respectively.

**TABLE 3.** Torque and rotor flux ripple for PCC and PTC - simulation results.

Ripple	PCC		PTC	
	$T_e$	$\lambda_r$	$T_e$	$\lambda_r$
$\omega_r^* = 270$	12.38%	2.73%	7.21%	2.17%
$\omega_r^* = 300$	12.20%	2.66%	7.75%	2.16%
$\omega_r^* = 340$	12.81%	2.86%	7.32%	2.30%

As explained before, for results concerning harmonic distortion, the THD values can be obtained in the conference paper [26]. It is shown that PCC has a lower THD in all scenarios with an average of 44% lower in stator current and 49% lower in rotor current compared to PTC.

Therefore, PCC presents better quality in both rotor and stator currents when compared to PTC. And PTC, in turn, presents a better result of rotor flux and electromagnetic torque, with smaller ripples in relation to those observed for PCC.

## VII. EXPERIMENTAL RESULTS

Experimental results for the DFIG-DC system are presented comparing PCC and PTC methods. Fig. 5 shows the experimental setup and Fig. 6 describes the experimental setup scheme. The computer applies the program to the Digital Signal Processor (DSP) TMS320F28335, which processes and controls the system signals. The oscilloscope used was Agilent, model DSO-X 3014A. In order to emulate a DC microgrid, an autotransformer feeds the DC bus through a diode bridge, keeping a constant voltage. Another autotransformer feeds a 550-W squirrel-cage induction motor (SCIM),

which has the function of imposing the mechanical torque of the system. The DFIG has its rotor and stator terminals connected to their respective power converters, RSC and SSR. There is also the DC bus, and a resistive load necessary to dissipate the power generated by the DFIG-DC, as there is no possibility of it being drained by the grid in this experiment.

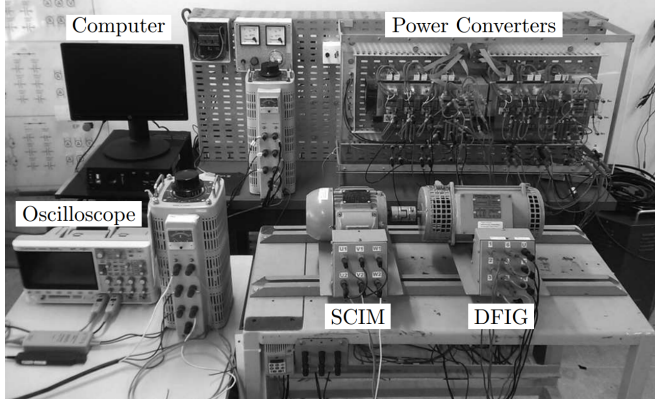


FIGURE 5. Experimental bench.

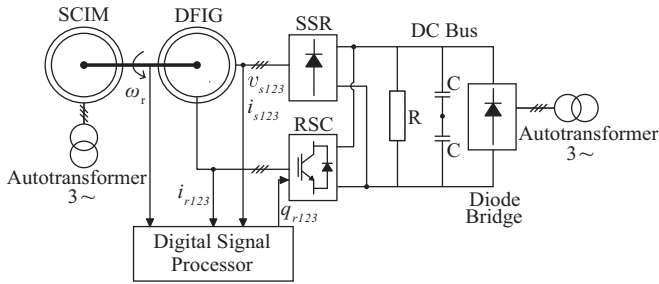


FIGURE 6. Experimental scheme.

Experiments were carried out for steady state, speed transients and parametric variations of the stator and rotor resistance, and of the magnetizing inductance.

### A. Steady-state results

The steady-state experimental results are illustrated in Figs. 7 to 9 acquired by the DSP and the oscilloscope. Three different experimental scenarios were carried out in order to compare the performance of PCC and PTC. The DC-link voltage was fixed at 250 V and the speed references were 270 rad/s (scenario 1), 300 rad/s (scenario 2) and 340 rad/s (scenario 3), respectively. For all cases, the synchronous frequency for PCC was fixed at 50 Hz, so that it was possible to observe the subsynchronous and supersynchronous behavior of the machine. Furthermore, the rotor flux for PTC was fixed at its nominal value of 0.93 Wb.

#### 1) Scenario 1

Figs. 7(a) and 7(b) show the steady-state rotor speed for PCC and PTC, respectively. Both techniques manage to regulate

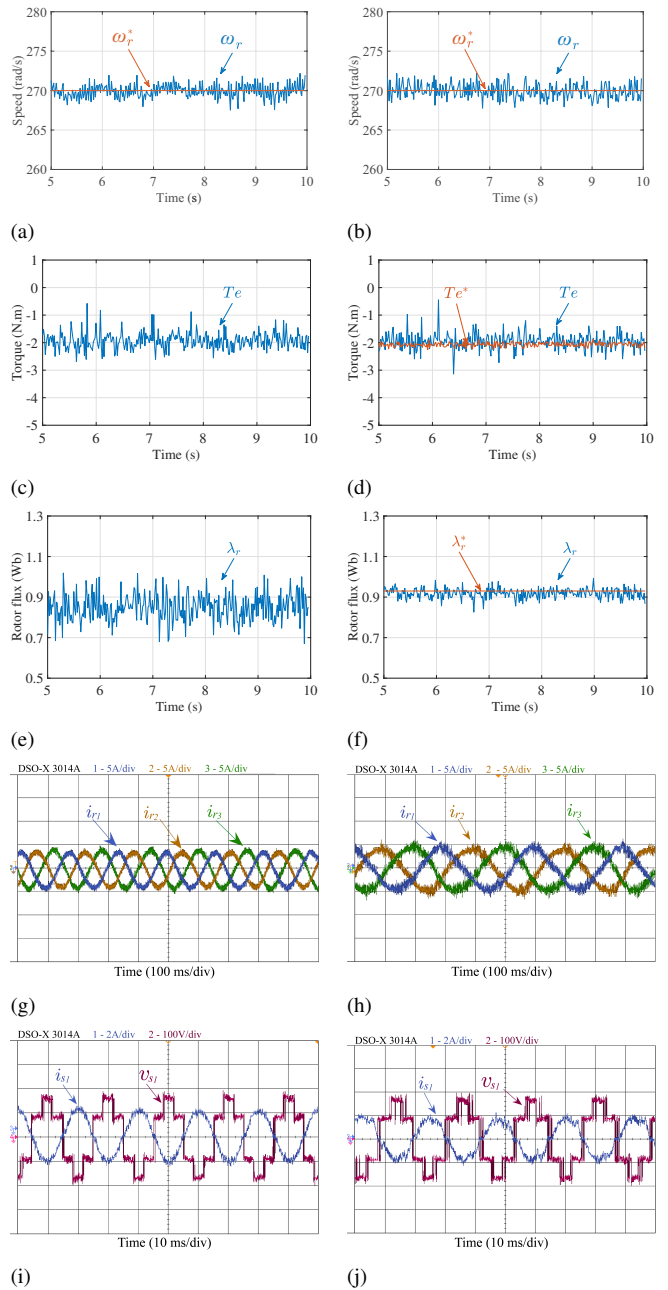


FIGURE 7. Experimental results for steady-state predictive control for  $\omega_r=270\text{rad/s}$  (scenario 1). (a) PCC machine speed. (b) PTC machine speed. (c) PCC torque. (d) PTC torque. (e) PCC rotor flux. (f) PTC rotor flux. (g) PCC rotor phase current. (h) PTC rotor phase current. (i) PCC stator phase voltage and phase current. (j) PTC stator phase voltage and phase current.

properly the rotor speed to the reference of 270 rad/s, making the system operate below the synchronous speed in the subsynchronous mode.

The electromagnetic torque of both methods presents similar behavior with an average of -2 N.m, as shown in Fig. 7(c), for PCC, and Fig. 7(d), for PTC. The rotor flux is shown in Figs. 7(e) and 7(f) for PCC and PTC, respectively.

Note that rotor flux was properly regulated with PTC, also presenting lower ripple compared to PCC.

Concerning the rotor currents, it is noticeable that their frequencies are different between PCC, Fig. 7(g), and PTC, Fig. 7(h), because the value of the synchronous speed varies depending on the operation point for PTC, while it is constant for PCC. Also, Figs. 7(i) and 7(j) show the stator current and voltage for PCC and PTC, respectively. It is possible to see that operation with unity power factor was assured.

## 2) Scenario 2

In this scenario, the machine operates at 300 rad/s for PCC and PTC, as shown in Figs. 8(a) and 8(b), respectively. It is noted that the speed is regulated adequately for both methods.

The electromagnetic torque is shown in Figs. 8(c) and 8(d) for PCC and PTC, respectively. The average value is close to -2 N.m. The rotor flux is shown in Figs. 8(e) and 8(f) for PCC and PTC, respectively. It can be seen that the flux control for PTC follows the reference and presents lower ripple compared to PCC.

The rotor currents, shown in Figs. 8(g), for PCC, and 8(h), for PTC, present smaller distortions in the former in relation to the latter. Furthermore, it can be seen that the frequency of the rotor current in PCC is much lower when compared to the previous scenario due to the fact that the machine speed is closer to synchronous speed, but still in subsynchronous mode. The frequency of this current in PTC is approximately the same as the previous one. However, the sequence of the phases is different, which proves that it has switched to supersynchronous mode. As for stator current and voltage, in both cases, they present a  $180^\circ$  phase difference between them, with the PCC presenting better current quality. The result of these variables for PCC can be seen in Fig. 8(i) and for PTC in Fig. 8(j).

## 3) Scenario 3

Figs. 9(a) and 9(b) show the machine speed and its reference for 340 rad/s for PCC and PTC, respectively. Both adjust the rotor speed properly. The electromagnetic torque can be visualized in Figs. 9(c) and 9(d) for PCC and PTC, respectively. The rotor flux is shown in Figs. 9(e) and 9(f) for PCC and PTC, respectively. PTC continues to present lower ripple than PCC.

Through the rotor currents, shown in Figs. 9(g) and 9(h) for PCC and PTC, respectively, it is possible to state that the machine is operating in supersynchronous mode, due to the change in the phase sequence when compared to scenario 1. In addition, it is observed that the frequency of the currents in PTC is very high, as it has moved even further away from the synchronous speed. The stator voltage and current can be seen in Fig. 9(i), for PCC, and in Fig. 9(j), for PTC.

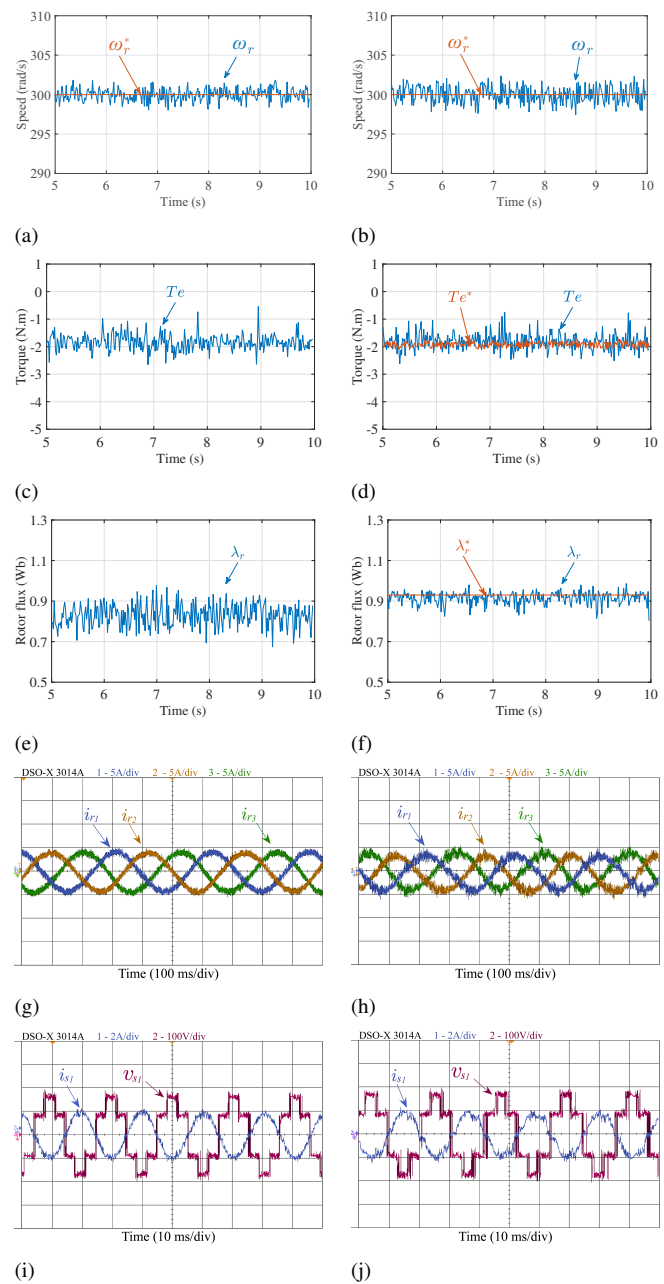


**FIGURE 8. Experimental results for steady-state predictive control for  $\omega_r=300\text{rad/s}$  (scenario 2). (a) PCC machine speed. (b) PTC machine speed. (c) PCC torque. (d) PTC torque. (e) PCC rotor flux. (f) PTC rotor flux. (g) PCC rotor phase current. (h) PTC rotor phase current. (i) PCC stator phase voltage and phase current. (j) PTC stator phase voltage and phase current.**

As in previous scenarios, unity power factor is guaranteed. The results of this scenario are also compatible with the simulation shown in the conference paper [26].

For the analysis of the torque and rotor flux ripple, an extra steady-state experiment was performed with more sample points (1000 points) in a shorter period of time (total of 0.1 seconds). Table 4 reports these values for PCC and PTC. It can be seen that PTC presents lower values of both torque

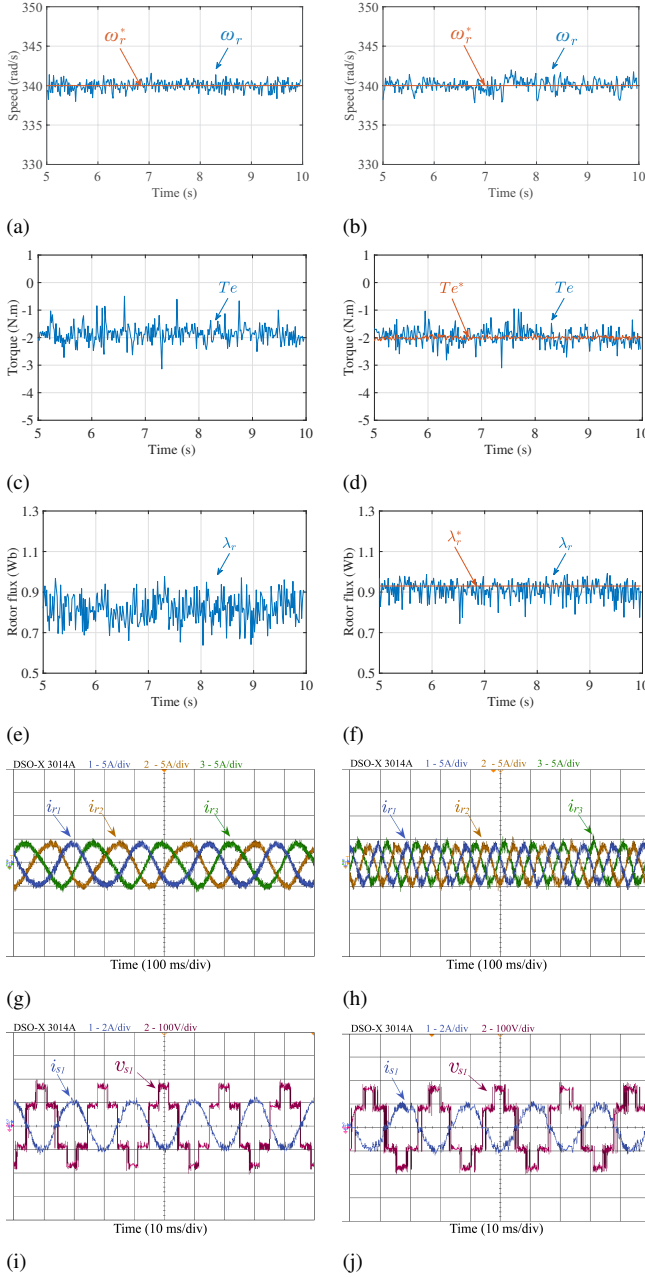


**FIGURE 9. Experimental results for steady-state predictive control for  $\omega_r=340\text{rad/s}$  (scenario 3). (a) PCC machine speed. (b) PTC machine speed. (c) PCC torque. (d) PTC torque. (e) PCC rotor flux. (f) PTC rotor flux. (g) PCC rotor phase current. (h) PTC rotor phase current. (i) PCC stator phase voltage and phase current. (j) PTC stator phase voltage and phase current.**

and flux ripple in all scenarios, confirming the simulation results.

Table 5 shows the average switching frequency ( $\bar{f}_{sw}$ ), and the stator and rotor currents THD for each scenario and each strategy. It is noted that PCC obtained a lower THD in all scenarios for both rotor and stator currents in relation to PTC. This demonstrates that current control has the advantage of generating better current quality. For the average switching

**TABLE 4. Torque and rotor flux ripple from PCC and PTC - experimental results.**

Ripple Scenario	PCC		PTC	
	$T_e$	$\lambda_r$	$T_e$	$\lambda_r$
1	27.17%	8.36%	24.99%	2.27%
2	31.15%	6.28%	25.32%	3.13%
3	37.35%	9.20%	27.72%	3.67%

**TABLE 5. Average switching frequency and stator and rotor currents THD for PCC and PTC - experimental results.**

Scenario	PCC			PTC		
	THD		$\bar{f}_{sw}$	THD		$\bar{f}_{sw}$
	$I_s$	$I_r$	kHz	$I_s$	$I_r$	kHz
1	35.1%	20.7%	2.14	40.1%	29.4%	2.02
2	36.4%	20.3%	2.08	40.6%	30.4%	1.94
3	43.3%	23.0%	2.14	44.2%	27.3%	1.99

frequencies, it can be seen that there is no significant change between each scenario, nor between the strategies.

Therefore, it is concluded, regarding the experimental results in steady state, that PCC obtained better performance in terms of quality of rotor and stator currents, while PTC presented better results in terms of torque and flux ripple. Both strategies managed to control the speed of the machine in all scenarios, whether configured in subsynchronous or supersynchronous mode, in addition to obtaining unity power factor. The results of experimental scenarios 1 and 3 are compatible with the simulations shown in the conference paper [26], and those of scenario 2 are in full accordance with the simulation results presented in Fig. 4.

**B. Transient-state results**

The system was also evaluated under speed transients, changing the reference speed from 270 rad/s to 340 rad/s and, a few seconds later, to 300 rad/s. The bus voltage used was 250V, PTC reference rotor flux was set at 0.93 Wb, PCC synchronous frequency was 50 Hz.

Fig. 10 shows the results for the case in which the system is submitted to speed step variations, acquired by the DSP and the oscilloscope. Initially the reference speed is 270 rad/s until eight seconds. At this point it is changed to 340 rad/s and, in eleven seconds, changed to 300 rad/s, as can be seen in Fig. 10(a) and 10(b) for PCC and PTC, respectively. It is noted that both techniques present a quick response to speed variations. The high undershoot in the PCC at the instant of speed reduction is noteworthy.

The electromagnetic torque, at times of speed variation, presents different behaviors as can be seen in Figs. 10(c) and 10(d) for PCC and PTC, respectively. When the speed increases, the torque tends to be positive. However, the control limits it to zero to ensure energy generation until the reference speed is reached. At the moment of changing the speed reference to a lower value, the torque presents a high negative peak. PTC has a lower value, around -7.5 N.m,

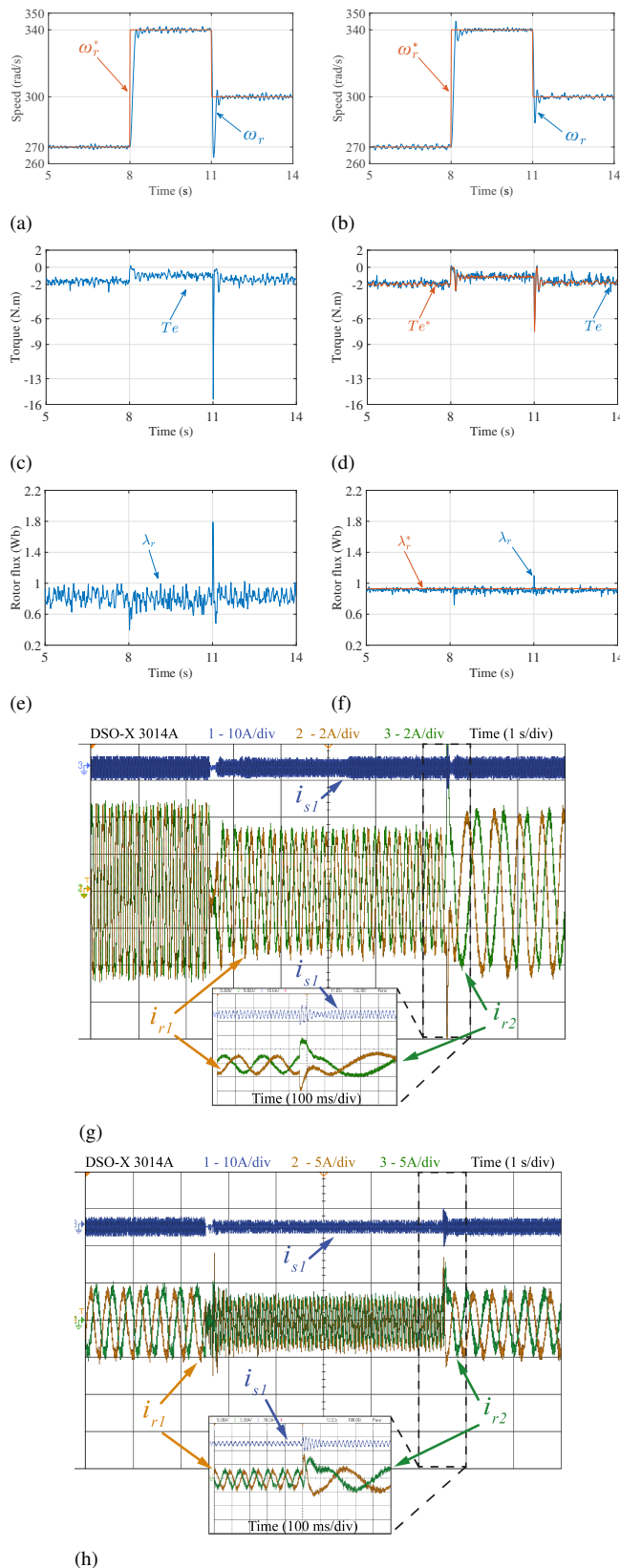


FIGURE 10. Experimental results of predictive control during speed transient. (a) PCC machine speed. (b) PTC machine speed. (c) PCC torque. (d) PTC torque. (e) PCC rotor flux. (f) PTC rotor flux. (g) PCC rotor and stator phase current. (h) PTC rotor and stator phase current.

while PCC has twice the value, around -15 N.m. This fact shows the good functioning of the torque control.

Another fact that can be noted is that there is a difference in the average value of the torque during the steady state of the three speeds. This occurred because, during this experiment, there was no change in the voltage imposed on the primary machine, and thus, there was no regulation of the mechanical torque, unlike the steady state results, in which this voltage was modified to adjust the electromagnetic torque to -2 N.m.

Figs. 10(e) and 10(f) show the rotor flux of PCC and PTC during the transient, respectively. A peak can be noted at the time of the speed decrease (in eleven seconds) that is quite high for PCC, around 1.8 Wb, and much lower for PTC, around 1.1 Wb.

Finally, the rotor and stator currents, during the transition, can be visualized in Figs. 10(g) and 10(h), together with the zoom in the second transition, for PCC and PTC, in that order. As for the rotor currents, it can be seen that the variation in speed caused their frequency to change for each steady state operation point. In PCC, as the synchronous speed is fixed in 314 rad/s, when the system operates in subsynchronous mode (first and third operation point) there is a sequence of current phases that differs from the sequence in supersynchronous mode (second operation point). This phenomenon becomes more noticeable when observing the zoom at the moment of the transition from 340 rad/s to 300 rad/s. Furthermore, the closer to synchronous speed, the lower the frequency, as can be seen for 300 rad/s.

In PTC, a frequency variation in rotor currents also occurs. Looking more closely, it can be seen that the first operation point presents a different sequence of phases than the other two. This indicates that the synchronous speed under these conditions is between 270 rad/s and 300 rad/s. Furthermore, a difference in the amplitude of the rotor currents is noted, which is due to the variation of the electromagnetic torque.

As for the stator current, PCC has the same frequency (50 Hz) for any speed value and its amplitude has a linear relationship with the torque, and thus, with the generated power. In PTC, the stator current varies slightly in frequency in each operation point. And as for amplitude, it is also linearly modified by the torque, as in PCC. It is worth to point out that there is a difference in the scale of the rotor current in Figure 10(g) and 10(h) which causes a visual difference between them.

### C. Parametric variations

The machine's parameters are obtained by experimental tests designed for this purpose. However, these parameters may vary depending on the operation point and temperature. Therefore, it is important to verify the robustness of control techniques in case there are errors or variations in the machine estimated parameters. In this way, the system was also experimented for parametric variations of stator resistance ( $r_s$ ), rotor resistance ( $r_r$ ) and magnetizing inductance ( $l_m$ ),

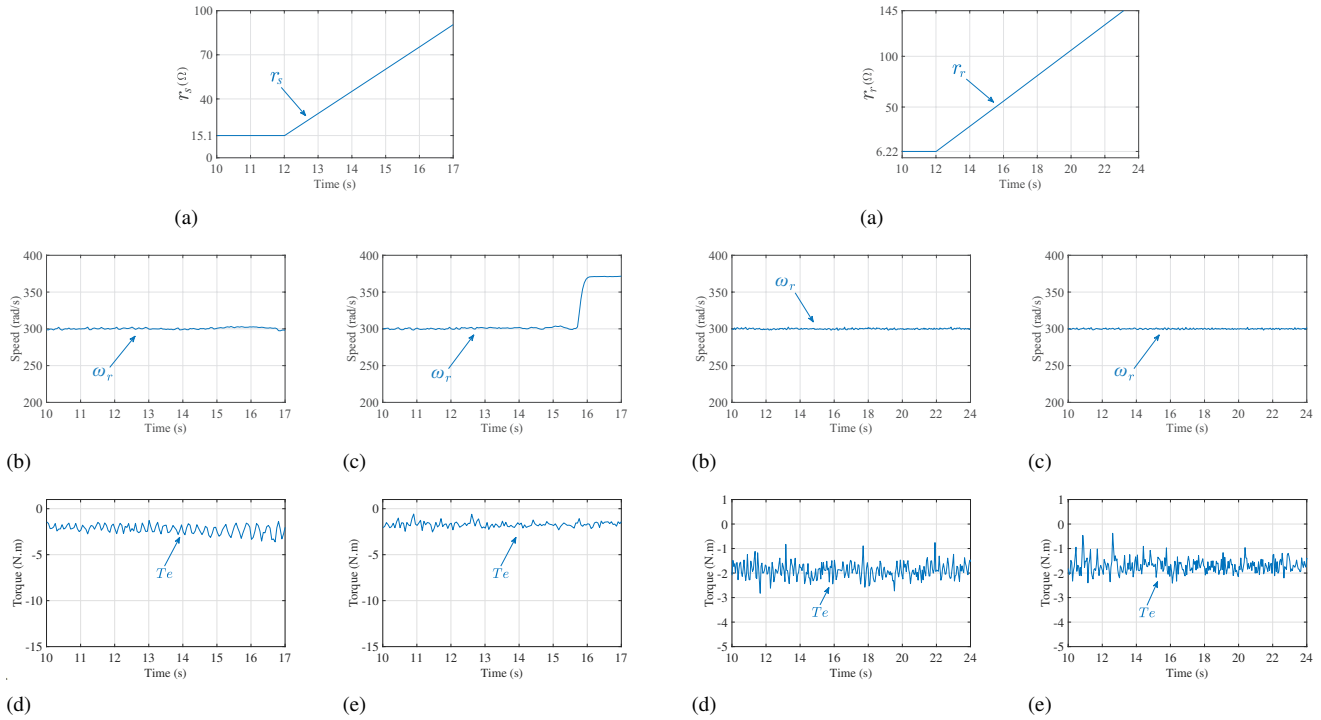


**FIGURE 11. Experimental results by varying  $r_s$ . (a) Variation  $r_s$ . (b) PCC machine speed. (c) PTC machine speed. (d) PCC torque. (e) PTC torque.**

where the parameter values used in the control algorithms were modified linearly with the purpose of verifying the behavior of the methods when the parameters had different values from the real ones present in the machine. The DC bus voltage used in these experiments was 250 V and the speed was 300 rad/s. PTC reference rotor flux was set at 0.93 Wb, PCC synchronous frequency was 50 Hz.

1) Stator resistance

The behavior of the system for the variation in stator resistance can be seen in Fig. 11. After the system reaches steady state, at the time of 12 seconds the value of the parameter begins to be altered in the control algorithm, as seen in Fig. 11(a).

It is noted that when PCC is employed, despite the increase of torque amplitude with high values of stator resistance, Fig. 11(d), the system in general does not lose speed control for the considered parametric variation band, as illustrated in Fig. 11(b). However, for PTC, the system loses control when the stator resistance reaches values above 68Ω (350% above the estimated value), as can be seen in Fig. 11(c), although the torque remains controlled, Fig. 11(e). With this, it can be stated that PTC was robust up to 350% of the estimated stator resistance value, and that PCC can reach greater levels of variation without losing control of the system.

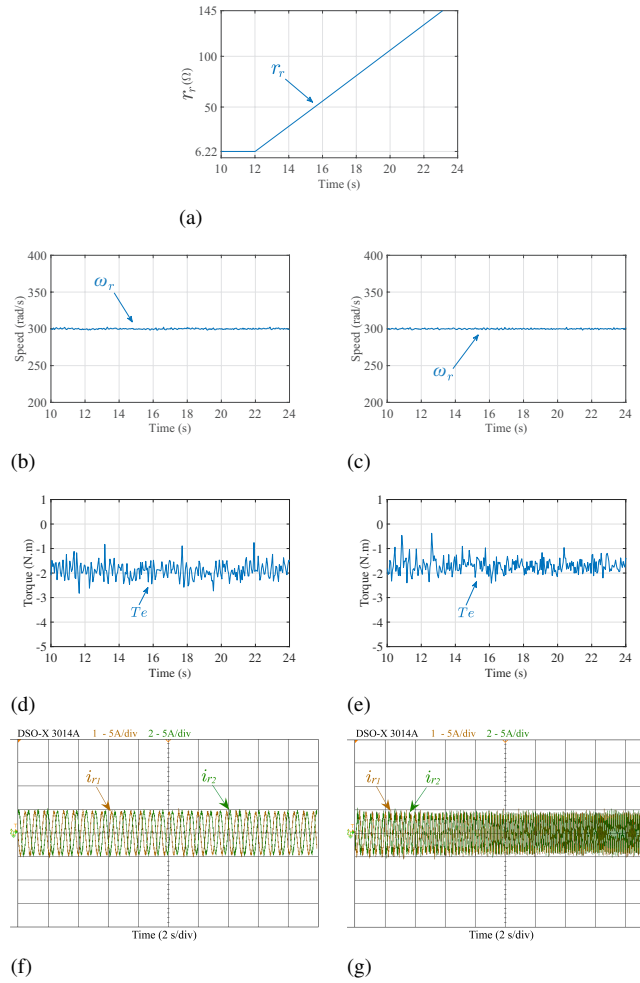


**FIGURE 12. Experimental results by varying  $r_r$ . (a) Variation  $r_r$ . (b) PCC machine speed. (c) PTC machine speed. (d) PCC torque. (e) PTC torque. (f) PCC rotor phase current. (g) PTC rotor phase current.**

2) Rotor resistance

The system’s response to variation in rotor resistance can be seen in Fig. 12. Similarly to the previous case, the value of the parameter begins to be altered in the control algorithm at the time of 12 seconds, as shown in Figs. 12(a).

It can be seen that the increase in rotor resistance from 6.22 Ω to 143 Ω (increase of 2300%) did not change the speed and torque provided by PCC, as shown in Figs. 12(b) and 12(d) respectively. The same is attested for PTC, as shown in Figs. 12(c) and 12(e).

Finally, the curves of the rotor currents were inserted exclusively in this scenario, Figs. 12(f) and 12(g) for PCC and PTC respectively, in order to prove that the system remains controlled, even with a high change in the parameter  $r_r$ . However, it can be seen that the modification in the value of the rotor resistance increases the frequency of the rotor currents in PTC. This implies that the synchronous speed changes as a function of this variation. Therefore, it is concluded that the two control methods are robust to the parametric variation of the rotor resistance for the

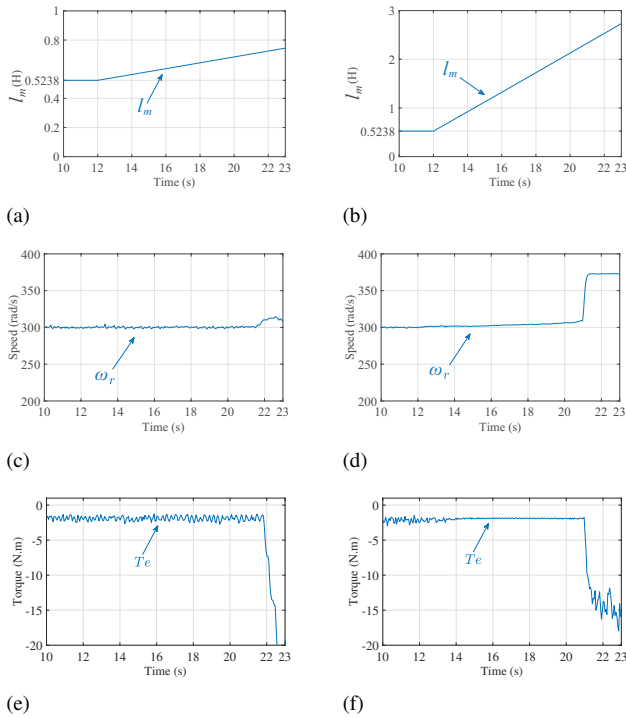


**FIGURE 13. Experimental results by varying  $l_m$ . (a) Variation  $l_m$  PCC. (b) Variation  $l_m$  PTC. (c) PCC machine speed. (d) PTC machine speed. (e) PCC torque. (f) PTC torque.**

implemented system, but PCC presents the advantage that there is no change in any other parameter.

### 3) Magnetizing inductance

Fig. 13 shows the results for the variation of the system's magnetizing inductance for PCC and PTC. At the time of 12 seconds the value of the parameter begins to be altered in the control algorithm, as seen in Fig. 13(a) and 13(b) for PCC and PTC, respectively. Unlike the previous cases, in this test the parameter grows in different proportions in each strategy. The reason for this is that the two methods diverge at different times, and to illustrate this, this modification was necessary.

For PCC, with approximately 50% of  $l_m$  variation above the estimated value, the system diverges as can be seen in Fig. 13(c) and 13(e), for the speed and electromagnetic torque, respectively. For PTC, the system diverges, as shown in Fig. 13(d) and 13(f), for the speed and electromagnetic torque, respectively, with an increase of  $l_m$  of 300%, proving to be more robust when compared to PCC. Therefore, it is concluded that PTC is more robust as it can keep the system stable for higher magnetizing inductance parametric errors than PCC.

Table 6 summarizes the comparison between PCC and PTC performed across the paper.

**TABLE 6. Comparison between PCC and PTC.**

Feature	PCC	PTC
Stator and rotor THD	Lower	Higher
Flux ripple	Higher	Lower
Torque ripple	Higher	Lower
Dynamic response	Fast	Fast
Robustness to variation in $r_s$	Higher	Lower
Robustness to variation in $r_r$	Higher	Medium
Robustness to variation in $l_m$	Lower	Higher
Voltage sensors	Not necessary	Necessary
Synchronous speed	Fixed	Variable

## VIII. CONCLUSIONS

A comparison between the predictive current control and predictive flux and torque control methods implemented in the DFIG-DC system was provided in this paper. Additionally, the operation and equations of PCC and PTC utilized in this system were explained in detail, also covering the speed control, and the selection of the switching states.

Considering the steady-state results obtained from simulations and experiments, the two control methods showed similar performance for different scenarios. The most notable differences in the simulation and experiment results were that PCC shows better current quality in both the rotor and stator, while PTC shows better results in rotor flux and electromagnetic torque, with lower ripple.

For speed transient analysis, both control methods demonstrate a good dynamic response. The most significant differences between them are observed in the lower variations in electromagnetic torque and rotor flux of PTC when the system is submitted to speed steps. Regarding the parametric variation of stator resistance, PCC is more robust compared to PTC. For rotor resistance, both methods maintain stability even with variations up to 2300% above the measured value. However, since PTC exhibits variations in rotor current frequency throughout the test, PCC is more robust in this situation. The variation in magnetizing inductance, on the other hand, causes the system to lose control with both strategies. Nevertheless, PTC proves to be more robust as it maintains control under larger variations compared to PCC.

Finally, PCC proves to be more advantageous than PTC mainly because it does not require voltage sensors, which reduces the cost of the system and presents a well-defined frequency and synchronous speed, making it simpler to determine the operating mode between subsynchronous and supersynchronous.

As future work, studies must be carried out to evaluate the robustness of DFIG-DC with FCS-MPC methods under open-phase and open-switch faults.

## ACKNOWLEDGMENT

The authors would like to thank PPGEE-UFPB, DEE-UFPB, grant #2021/07 Paraíba State Research Foundation (FAPESQ), the Agencia Nacional de Investigación y Desar-

rollo (ANID) FONDECYT Regular grant number 1220556, the Research Project PINV01-743 of the Consejo Nacional de Ciencia y Tecnología (CONACYT), ENNOBLE-R02401, and IRCF project from the University of Nottingham for the financial support.

#### AUTHOR'S CONTRIBUTIONS

**L.F.M.LUCENA:** Data Curation, Formal Analysis, Investigation, Methodology, Validation, Visualization, Writing – Review & Editing. **V.F.M.B.MELO:** Conceptualization, Data Curation, Formal Analysis, Investigation, Methodology, Supervision, Writing – Original Draft, Writing – Review & Editing. **N.ROCHA:** Funding Acquisition, Project Administration, Supervision, Visualization. **R.D.C.FERREIRA:** Visualization. **M.RIVERA:** Visualization, Writing – Review & Editing.

#### PLAGIARISM POLICY

This article was submitted to the similarity system provided by Crossref and powered by iThenticate – Similarity Check.

#### REFERENCES

- [1] E. Rodriguez-Diaz, M. Savaghebi, J. C. Vasquez, J. M. Guerrero, "An overview of low voltage DC distribution systems for residential applications", in *2015 IEEE 5th International Conference on Consumer Electronics - Berlin (ICCE-Berlin)*, pp. 318–322, 2015, doi:10.1109/ICCE-Berlin.2015.7391268.
- [2] T. Dragičević, X. Lu, J. C. Vasquez, J. M. Guerrero, "DC Microgrids—Part II: A Review of Power Architectures, Applications, and Standardization Issues", *IEEE Transactions on Power Electronics*, vol. 31, no. 5, pp. 3528–3549, 2016, doi:10.1109/TPEL.2015.2464277.
- [3] N. K.K., J. N. S., V. Jadoun, "An overview of DC Microgrid with DC distribution system for DC loads", *Materials Today: Proceedings*, vol. 51, 06 2021, doi:10.1016/j.matpr.2021.06.093.
- [4] A. Akhbari, M. Rahimi, M. Khooban, "Direct current grid-based doubly-fed induction generator wind turbines: Real-time control and stability analysis", *IET Power Electronics*, vol. 15, 09 2022, doi:10.1049/pel2.12299.
- [5] T. Ahmed, K. Nishida, M. Nakaoka, "A Novel Stand-Alone Induction Generator System for AC and DC Power Applications", *Industry Applications, IEEE Transactions on*, vol. 43, pp. 1465 – 1474, 12 2007, doi:10.1109/TIA.2007.908210.
- [6] M. Tazil, V. Kumar, R. C. Bansal, S. Kong, Z. Y. Dong, W. Freitas, H. D. Mathur, "Three-phase doubly fed induction generators: an overview", *IET Electric Power Applications*, vol. 4, pp. 75–89, 2010.
- [7] G. D. Marques, M. F. Iacchetti, "DFIG Topologies for DC Networks: A Review on Control and Design Features", *IEEE Transactions on Power Electronics*, vol. 34, no. 2, pp. 1299–1316, 2019, doi:10.1109/TPEL.2018.2829546.
- [8] N. Holtmark, H. J. Bahirat, M. Molinas, B. A. Mork, H. K. Hoidalén, "An All-DC Offshore Wind Farm With Series-Connected Turbines: An Alternative to the Classical Parallel AC Model?", *IEEE Transactions on Industrial Electronics*, vol. 60, no. 6, pp. 2420–2428, 2013, doi:10.1109/TIE.2012.2232255.
- [9] P. Karlsson, J. Svensson, "DC bus voltage control for a distributed power system", *IEEE Transactions on Power Electronics*, vol. 18, no. 6, pp. 1405–1412, 2003, doi:10.1109/TPEL.2003.818872.
- [10] T. Dragičević, X. Lu, J. C. Vasquez, J. M. Guerrero, "DC Microgrids—Part I: A Review of Control Strategies and Stabilization Techniques", *IEEE Transactions on Power Electronics*, vol. 31, no. 7, pp. 4876–4891, 2016, doi:10.1109/TPEL.2015.2478859.
- [11] M. G. Jahromi, G. Mirzaeva, S. D. Mitchell, D. Gay, "Powering Mobile Mining Machines: DC Versus AC Power", *IEEE Industry Applications Magazine*, vol. 22, no. 5, pp. 63–72, 2016, doi:10.1109/MIAS.2015.2459082.
- [12] B. Zahedi, L. E. Norum, "Modeling and Simulation of All-Electric Ships With Low-Voltage DC Hybrid Power Systems", *IEEE Transactions on Power Electronics*, vol. 28, no. 10, pp. 4525–4537, 2013, doi:10.1109/TPEL.2012.2231884.
- [13] A. Gundavarapu, H. Misra, A. K. Jain, "Direct Torque Control Scheme for DC Voltage Regulation of the Standalone DFIG-DC System", *IEEE Transactions on Industrial Electronics*, vol. 64, no. 5, pp. 3502–3512, 2017, doi:10.1109/TIE.2016.2644623.
- [14] G. Iwański, M. Piwek, G. Dauksha, "Doubly Fed Induction Machine-Based DC Voltage Generator with Reduced Oscillations of Torque and Output Voltage", *Energies*, vol. 16, no. 2, 2023, URL: <https://www.mdpi.com/1996-1073/16/2/814>.
- [15] M. F. Iacchetti, G. D. Marques, R. Perini, "A Scheme for the Power Control in a DFIG Connected to a DC Bus via a Diode Rectifier", *IEEE Transactions on Power Electronics*, vol. 30, no. 3, pp. 1286–1296, 2015, doi:10.1109/TPEL.2014.2317947.
- [16] S. Kouro, P. Cortes, R. Vargas, U. Ammann, J. Rodriguez, "Model Predictive Control—A Simple and Powerful Method to Control Power Converters", *IEEE Transactions on Industrial Electronics*, vol. 56, no. 6, pp. 1826–1838, 2009, doi:10.1109/TIE.2008.2008349.
- [17] F. Wang, S. Li, X. Mei, W. Xie, J. Rodríguez, R. M. Kennel, "Model-Based Predictive Direct Control Strategies for Electrical Drives: An Experimental Evaluation of PTC and PCC Methods", *IEEE Transactions on Industrial Informatics*, vol. 11, no. 3, pp. 671–681, 2015, doi:10.1109/TII.2015.2423154.
- [18] V. S. S. Pavan Kumar Hari, G. Narayanan, "Theoretical and Experimental Evaluation of Pulsating Torque Produced by Induction Motor Drives Controlled With Advanced Bus-Clamping Pulsewidth Modulation", *IEEE Transactions on Industrial Electronics*, vol. 63, no. 3, pp. 1404–1413, 2016, doi:10.1109/TIE.2015.2494530.
- [19] J. Song-Manguelle, S. Schröder, T. Geyer, G. Ekemb, J.-M. Nyobe-Yome, "Prediction of Mechanical Shaft Failures Due to Pulsating Torques of Variable-Frequency Drives", *IEEE Transactions on Industry Applications*, vol. 46, no. 5, pp. 1979–1988, 2010, doi:10.1109/TIA.2010.2057397.
- [20] X. Han, A. B. Palazzolo, "VFD Machinery Vibration Fatigue Life and Multilevel Inverter Effect", *IEEE Transactions on Industry Applications*, vol. 49, no. 6, pp. 2562–2575, 2013, doi:10.1109/TIA.2013.2265871.
- [21] B. Zhu, K. Rajashekhara, H. Kubo, "A Comparison between Current Based and Flux/Torque Based Model Predictive Control Methods for Open-End Winding Induction Motor Drives", *IET Electric Power Applications*, vol. 11, 05 2017, doi:10.1049/iet-epa.2016.0517.
- [22] L. M. d. Oliveira, V. F. M. B. Melo, G. F. da Paz, F. V. Rocha, E. L. L. Fabricio, "Experimental Assessment of Predictive Current Control Applied to Induction Machine Drive Systems Operating Under Single-Phase Open-Circuit Fault", *Eletrônica de Potência*, vol. 29, Mar. 2024, doi:10.18618/REP.2024.1.0011.
- [23] F. Guedes, N. Rocha, A. Maciel, A. Sguarezi, "Finite-Set Model Predictive Direct Power Control for DFIG with Reduced Number of Voltage Vectors", *Eletrônica de Potência*, vol. 28, pp. 1–11, 03 2023, doi:10.18618/REP.2023.1.0025.
- [24] S. Bayhan, H. Abu-Rub, O. Ellabban, "Sensorless Model Predictive Control Scheme of Wind-Driven Doubly Fed Induction Generator in DC Microgrid", *IET Renewable Power Generation*, 01 2016, doi:10.1049/iet-rpg.2015.0347.
- [25] S. M. A. Cruz, G. D. Marques, P. F. C. Gonçalves, M. F. Iacchetti, "Predictive Torque and Rotor Flux Control of a DFIG-DC System for Torque Ripple Compensation and Loss Minimization", *IEEE Transactions on Industrial Electronics*, vol. 65, pp. 9301–9310, 2018, doi:10.1109/TIE.2018.2818667.
- [26] L. F. M. De Lucena, V. F. M. B. Melo, N. Rocha, R. Da Cruz Ferreira, "Comparison Between Predictive Current and Predictive Torque Control Applied to a Doubly-Fed Induction Generator System for Connection to DC Microgrids", in *2023 IEEE 8th Southern Power Electronics Conference and 17th Brazilian Power Electronics Conference (SPEC/COBEP)*, pp. 1–6, 2023, doi:10.1109/SPEC56436.2023.10408100.
- [27] Y. Xiao, B. Fahimi, M. A. Rotea, Y. Li, "Multiple Reference Frame-Based Torque Ripple Reduction in DFIG-DC System", *IEEE Transactions on Power Electronics*, vol. 35, no. 5, pp. 4971–4983, 2020, doi:10.1109/TPEL.2019.2941957.
- [28] P. Cortes, J. Rodriguez, C. Silva, A. Flores, "Delay Compensation in Model Predictive Current Control of a Three-Phase Inverter", *IEEE*

- Transactions on Industrial Electronics*, vol. 59, no. 2, pp. 1323–1325, 2012, doi:10.1109/TIE.2011.2157284.
- [29] C. Lascu, I. Boldea, F. Blaabjerg, W. Chen, “A class of flux observers for doubly-fed induction generators used in small power wind generation systems”, in *2013 IEEE Energy Conversion Congress and Exposition*, pp. 2289–2295, 2013, doi:10.1109/ECCE.2013.6646993.
- [30] C. Wu, P. Cheng, H. Nian, F. Blaabjerg, “Rotor Current Oriented Control Method of DFIG-DC System Without Stator Side Sensors”, *IEEE Transactions on Industrial Electronics*, vol. PP, pp. 1–12, 2019, doi:10.1109/TIE.2019.2956415.
- [31] C. Wu, P. Cheng, Y. Ye, F. Blaabjerg, “A Unified Power Control Method for Standalone and Grid-Connected DFIG-DC System”, *IEEE Transactions on Power Electronics*, vol. 35, no. 12, pp. 12663–12667, 2020, doi:10.1109/TPEL.2020.2996267.
- [32] V. Yaramasu, B. Wu, *Model Predictive Control of Wind Energy Conversion System*, chap. 3, pp. 91–116, John Wiley & Sons, Ltd, <https://onlinelibrary.wiley.com/doi/abs/10.1002/9781119082989.ch3>, 2017.

## BIOGRAPHIES

**Lucas Fabrício Medeiros de Lucena** received the B.S. and M.S degree in electrical engineering from the Federal University of Paraíba, João Pessoa, Brazil, in 2021 and 2023, respectively. He is currently working toward the Ph.D. degree in electrical engineering with the Federal University of Campina Grande, Campina Grande, Brazil. His research interests include power electronics, power quality systems and electrical drives.

**Victor Felipe Moura Bezerra Melo** received the B.S., M.S., and Ph.D. degrees in electrical engineering from the Federal University of Campina Grande, Campina Grande, Brazil, in 2012, 2013, and 2017, respectively. From October 2014 to June 2018, he was with the Federal Institute of Technology of Pernambuco, Afogados da Ingazeira, Brazil, where he was a Professor. Since June 2018, he has been with Renewable Energy Engineering Department, Federal University of Paraíba, João Pessoa, Brazil, where he is currently a Professor. His current research interests are multiphase drives, wind energy systems, and converter topologies.

**Nady Rocha** received the B.S., M.S. and Ph.D. degrees in electrical engineering from the Federal University of Campina Grande, Brazil, in 2006, 2008 and 2010, respectively. Since 2011, he has been with the Department of Electrical Engineering, Federal University of Paraíba, João Pessoa, where he is currently an Associate Professor of Electrical Engineering. His research interests include power electronics, renewable energy sources, and electrical drives.

**Ruben da Cruz Ferreira** received his B.S. degree in electrical engineering from the Federal University of Paraíba, João Pessoa, Brazil, in 2024. His research interests include power electronics, renewable energy sources and electrical drives.

**Marco Rivera** received his Electronic Civil Engineering degree in 2007 and M.Sc. in Engineering with a specialization in Electrical Engineering in 2008 from the Universidad de Concepción, Chile. He subsequently earned his Ph.D. in Electronic Engineering from the Universidad Técnica Federico Santa María in Chile, where his doctoral work was recognized with the prestigious “Premio Tesis de Doctorado Academia Chilena de Ciencias 2012” for the best Ph.D. thesis in exact and natural sciences. He served as the Director of the Laboratory of Energy Conversion and Power Electronics (LCEEP) at the Universidad de Talca, Chile, where he was a Full Professor in the Department of Electrical Engineering. In April 2023, he joined the Power Electronics, Machines and Control (PEMC) Research Institute at the University of Nottingham, UK. Currently, he also serves as the Director of the FlexElec Laboratory within the PEMC Research Institute. With a research portfolio encompassing power electronics, renewable energy integration, advanced control strategies, microgrids, and hybrid energy systems, Prof. Rivera’s work has had a profound impact on the development of advanced technologies for renewable energy and power electronics, earning him recognition as a leader in these domains.